PAPER • OPEN ACCESS

Measuring timing properties of thermal infrared cameras

To cite this article: Volker Schatz 2023 *Meas. Sci. Technol.* **34** 055407

View the article online for updates and enhancements.

Measuring timing properties of thermal infrared cameras

Volker Schatz

Fraunhofer IOSB, Gutleuthausstraße 1, 76275 Ettlingen, Germany

E-mail: volker.schatz∂iosb.fraunhofer.de

CrossMark

Abstract

A measurement setup and method is presented that serves to determine constants characterising the timing behaviour of thermal infrared cameras. A continuously rotating chopper wheel is used to periodically obscure and reveal the cutout of a mask plate. The exposed fraction of the cutout is the main measured quantity. Irregularities in the chopper wheel are determined from timestamps of the light beam detectors in the chopper head. The method is suitable for both kinds of thermal cameras, cooled cameras and microbolometer cameras, and for both snapshot and rolling-frame cameras. Example results are presented for a cooled snapshot camera and a rolling-frame microbolometer camera.

Keywords: thermal infrared camera, microbolometer, timing, calibration

(Some figures may appear in colour only in the online journal)

1. Introduction

In computer vision research today, sensor fusion plays an important part. A fair share of work on that topic includes data from thermal infrared cameras, e.g. [1–4]. Combining data from multiple sensors to a common data set requires referencing them in a common spatial coordinate system as well as on a common time scale. Thermal cameras are also being used or considered in reactive systems in various domains of application including security, aerial navigation and driver-assistance systems [5–10]. Tracking movement, either of the vehicle containing the camera or of a different object, requires assigning a time to the camera data used.

The state of the art for sensor systems for these applications is to trigger or timestamp all sensor data with a common clock. This is rarely mentioned, let alone considered critically. Commercial products like cameras are not primarily intended for scientific applications, and may exhibit internal delays and

other timing properties that are not always well documented. Time-sensitive applications could benefit greatly from a way to measure these properties and allow compensating for delays.

However, timing measurement and calibration is a tiny field even for video cameras, e.g. [11–13]. There is even less work on the timing of thermal infrared cameras, often as part of a larger investigation. Prior work has concentrated on microbolometer cameras, the less expensive kind, the operation of which is briefly described in section 3.2.

An investigation by Hopkinson *et al* [14] of sensors for use in a satellite contains the measurement of the response of a microbolometer infrared camera using a shutter. The shutter is operated at a random time and the known row offset of the rolling-frame camera is used to determine the response over time. The measurement is presented only briefly, and it is not discussed how the camera response profile is compensated for the profile of the non-instantaneous opening and closing of the mechanical shutter; and how the random time of the shutter operation is put in relation to the camera trigger time to obtain the result.

Danial's bachelor thesis [15] investigates a possible way of reducing motion blur of a microbolometer infrared camera. A chopper wheel is used to create an exposure interval outside which the scene is obscured from the camera. In a small part

of the work, the decay time of the camera is determined from a scene containing two blackbodies. The start and end of exposure of the scene is treated as instantaneous, and the row delay of the camera is ignored.

Peeters *et al* [16] present a measurement of the rolling-frame row delay of a microbolometer camera as well as the frame interval for various trigger modes, and a method to correct for them. A flash lamp is used to briefly heat up an aluminium plate, which is observed by the camera as it cools down to ambient temperature. The delay between individual pixels is obtained from the time of the maximum pixel value interpolated between camera frames using a fit function. The decay time of the camera is not measured, as that is not needed for the purpose of undoing the distortion of the images.

Waldron and Lohrmann [17] use a modulated CO_2 laser to illuminate the detector of a microbolometer camera without a lens, making their setup a thermal infrared variant of [12] in principle. They obtain very accurate results of the decay time and its variation between pixels. The row and overall trigger delay are not determined.

Decay times of microbolometer detectors are also often determined in work on bare detectors, e.g. [18–20]. These methods require access to the detector and are not applicable to complete cameras. They provide no information on the timing arising from the camera electronics and again treat only microbolometers, not photon detectors.

This work will present a general-purpose measurement method to determine the timing parameters of any thermal infrared camera. The measurement setup will be described in the following section. Example results from two cameras will be presented in section 3, one for a cooled camera and one for a microbolometer camera. Section 4 will discuss limitations and possible improvements of the measurement method, and section 5 will sum up the report.

2. Measurement setup

2.1. General

In order to determine the timing of thermal infrared sensors, the camera frames have to be related to a process with known timing. This was done by recording a camera image sequence of a chopper wheel rotating in front of a blackbody. Both the camera trigger and the synchronisation signal for the chopper controller were generated by the same custom circuit. This allowed to determine the timing relative to the trigger time.

The setup is displayed in figure 1(a). The camera views the chopper wheel in front of the blackbody as a background. The blackbody temperature was set to 5–10 K above or below room temperature in order to provide a good contrast with the chopper wheel. Both the chopper wheel and the blackbody require controller devices for operation, which are visible in the image. The type of chopper used was a Thorlabs MC2000B-EC with a wheel of type MC1F2; the type of blackbody was an eight inch CI Systems SR-800 R. The trigger generator will be described in detail in the following section on triggering. The signal driver merely serves to amplify a signal for timestamping.

The chopper wheel has two cutouts of 90° between its solid centre and the rim with slots for rotation control. For the timing measurements, a mask plate was attached to the chopper head behind the wheel, as can be seen in figure 1(b). The mask has a single 75° annular section cutout that is slightly narrower in the radial direction than the wheel cutouts. The overlap of the mask opening with a wheel cutout is the main measured quantity. Having a mask cutout of less than 90° provides angle intervals during which the opening is completely open or covered, which will be used for normalisation.

The surface of the chopper wheel is smooth enough to reflect infrared radiation. This causes the camera body or other warm objects to be mirrored in the camera images and makes it harder to distinguish the wheel from the blackbody background. This was prevented by putting a screen of corrugated fibreboard around the lens, the type of cardboard from which shipping boxes are made and which is a good thermal insulator due to its hollow structure.

As a precautionary optimisation, the cameras and the chopper head were attached to an aluminium rod using 3D-printed bases. They were positioned so as to approximately align the camera optical axis with the centre of the chopper wheel. Lens distortion is generally considered less significant in the azimuthal than the radial direction ([21] p. 328 top; [22] p. 189, section 7.4), so aligning the axes reduces the effect of lens distortion on the annular cutouts.

2.2. Synchronisation and trigger hardware

The chopper controller keeps the wheel rotation speed constant using one of the light beam detectors for the slots on the rim of the wheel. The outer set of two slots matches the large cutouts of the wheel and are called the application slots. For more accurate rotation control the inner set of 100 slots, the control slots, were used. Both slot circles and the corresponding detectors at the bottom can be seen in figure 1(b).

The external reference signal for the chopper controller was generated by the trigger generator. The controller in turn outputs the control slot edge detector signal, which was fed into the trigger generator to be timestamped. In order to have a starting point for the angular position of the chopper wheel, the signal from the application slot edge detector was tapped inside the controller, which cannot normally output both edge detector signals. It was fed through the signal driver and then also into the trigger generator for timestamping.

Figure 2 shows a schematic of the trigger generator and its connections. It contains two pulse generators with adjustable periods. One of them triggers the camera. The other provides the reference signal for the chopper rotation control and thereby determines the rotation speed of the wheel. The latter is active permanently so that the chopper can lock to it. The camera trigger is only activated during a measurement. At the start of a measurement, data acquisition is started shortly before triggering is activated to ensure the first recorded frame matches the first trigger timestamp.

During measurements, timestamps are generated for the camera trigger and signals from both detectors of the chopper
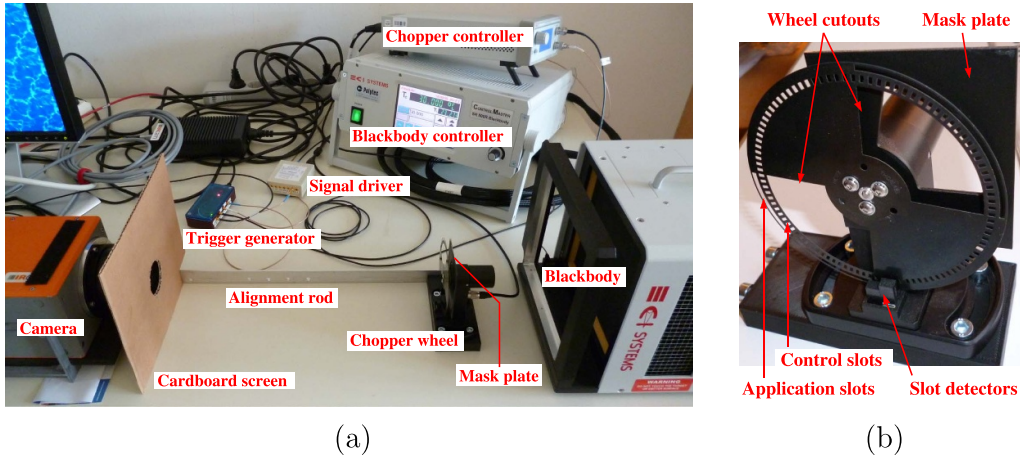
Figure 1. (a) Measurement setup excluding PC for camera recording and control. See text for description. (b) Chopper wheel and mask plate.
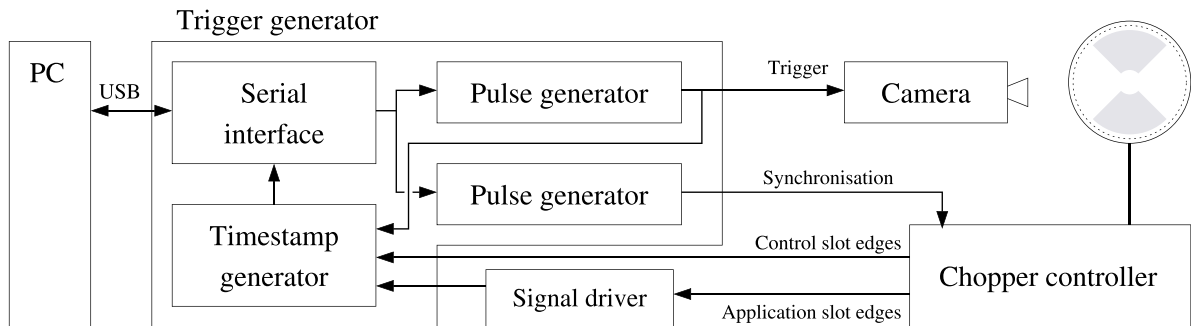
Figure 2. Simplified schematic of the trigger generator and of trigger and synchronisation signals. When triggering is active, timestamps are transmitted to the PC and recorded there.

wheel. The timestamps are values of a continually running counter in the trigger generator at the first clock cycle after a change in the signal. For the chopper signals, the signal edges marking the transition from cut out to solid at the detector are timestamped. In the case of the camera trigger, the timestamp is generated for the same edge that the camera accepts as a trigger.

The trigger generator was implemented as a custom circuit in a Field-Programmable Gate Array (FPGA), a Xilinx Spartan-3E. The FPGA is located on a small board (GODIL by OHO-Elektronik) that also contains a clock generator, a microcontroller, flash memory for the FPGA configuration and input/output level shifters. The microcontroller mediates between the universal serial bus (USB) and a serial interface whose counterpart is implemented in the FPGA. That way registers can be read and written and timestamps read by a PC via the USB.

2.3. Triggering scheme

In a timing measurement, one or multiple rotations of the chopper wheel are sampled at equidistant times with camera images. The simplest way to do that is to trigger one camera frame per chopper wheel rotation at increasing angles, but this has several drawbacks. In order to minimise motion blur,

the chopper wheel is operated at a rotation rate of approximately 3 Hz. Therefore sampling with decent time resolution at one frame per rotation takes a long time. Infrared cameras also need to perform detector non-uniformity corrections at intervals of the order of tens of minutes in order to preserve image quality. It is undesirable for a non-uniformity correction to occur during a measurement because it can cause jumps in pixel values.

These problems are avoided by triggering multiple camera frames per wheel rotation. The camera trigger period and the period of the chopper synchronisation reference signal are set in the trigger generator in units of FPGA clock cycles with the frequency $f = 49.152$ MHz. All time intervals derived from the trigger signals can be expressed as integers in units of clock cycles. C shall be the camera trigger period, T' the chopper reference signal period, T the duration of one wheel rotation, and δ the effective sampling interval.

Figure 3 shows a simple example. The blue intervals represent the rotations of the wheel. The effective sampling interval $\delta = \gcd(T, C)$ is smaller than C. Adjacent sampling points are not sampled in order. For example, the second sampling point is recorded at the eighth trigger because $\delta \equiv 7C \bmod T$.

For the example measurements presented below, approximate requirements were $T/\delta \approx 1000$ samples per rotation, a camera frame rate of $f/C \approx 30$ Hz and a rotation speed of
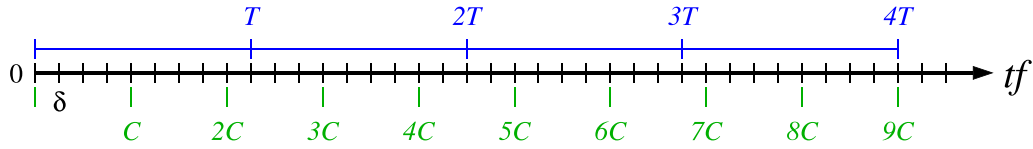
Figure 3. Toy example of sampling a T-periodic process with the sampling interval C to achieve the effective sampling interval δ. The time axis is discretised in steps of $1/f$, which is the unit of the interval quantities.
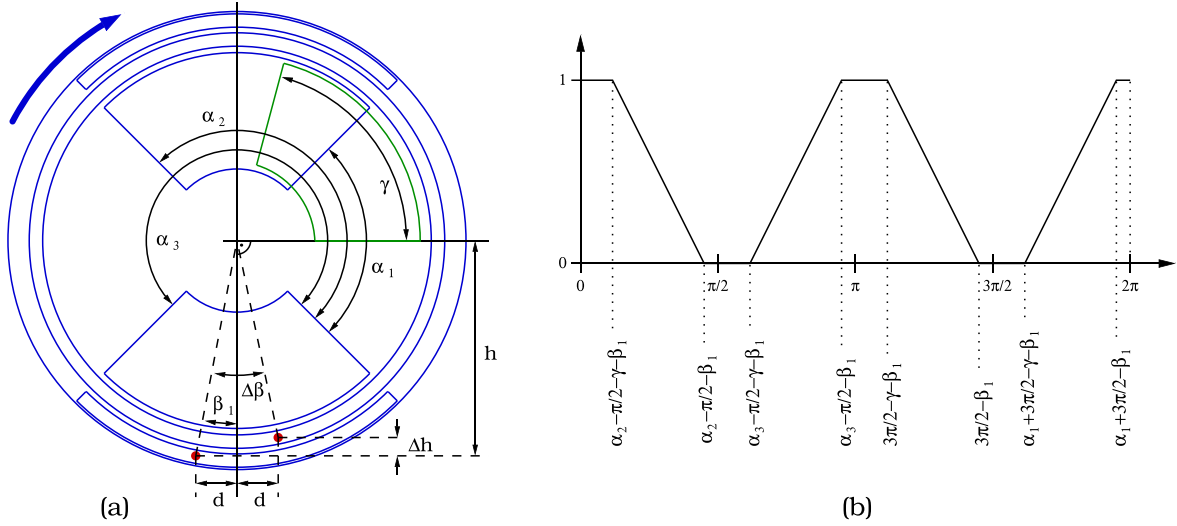
Figure 4. (a) Geometry of chopper wheel (blue), mask opening (green) and light beam detectors (red), not to scale. The wheel rotates clockwise as seen by the camera. (b) Model of uncovered fraction of mask opening depending on the wheel orientation angle and the parameters in (a).

$f/T \approx 3$ Hz. T is a multiple of 100 because there are 100 control slots in the wheel and the chopper synchronisation signal period $T' = T/100$ has to be an integer. T/δ and C/δ are relatively prime because $\delta = \gcd(T, C)$. They were chosen as $T/\delta = 1000$ and $C/\delta = 99$, which fulfils the number theoretic properties and the approximate ratio between the desired rotation speed and camera frame rate. Choosing $\delta = f/3000\,\mathrm{Hz} = 16\,384$ yields $f/T = 3$ Hz and $f/C = 30.303$ Hz. The duration of a measurement run is $1\,\mathrm{cm}(T, C)/f = 33$ s.

If an exact camera frame rate is required, the number of samples per rotation can no longer be chosen freely, and may most conveniently be chosen as a prime number. The computer algebra system PARI/GP from the University of Bordeaux [23], which specialises in number theory, has been very helpful in finding suitable trigger parameters.

2.4. Obtaining wheel angles from timestamps

The timestamps of the chopper edges are used to convert the camera trigger timestamps to wheel angles for each camera frame. The edges of the application slot circle corresponding to the large cutouts of the wheel are used to define the zero angle. For an ideal chopper wheel the two edges would be indistinguishable. Actually the chopper wheel is not perfectly symmetric and/or not perfectly centred on the chopper head. After averaging every other interval between these edges, the two intervals differ by more than a standard deviation, which

allows to distinguish the edges. The edge preceding the longer interval is chosen as the reference edge defining angle zero, and angles extend over the whole range $[0, 2\pi)$.

The chopper edge timestamps of the control slot circle are used to correct for the remaining inaccuracies in rotation uniformity. Using the fact that the angular distance between successive edges is $\pi/50$, the angles of camera frames are determined by linear interpolation between the control slot timestamps. As a consequence the angles of corresponding frames from different runs of the same measurement differ slightly.

2.5. Model of the chopper wheel

The main measured quantity will be the fraction of the mask opening that is exposed by the chopper wheel at a given angle. In order to be able to compare measurement results with a theoretical model, a number of parameters have to be determined. Figure 4(a) shows the geometry of the chopper wheel and related components. Importantly, the edge detector light beams are not at the same angle position, but differ by $\Delta\beta$.

The most important parameter is the angle offset β_1 of the light beam that defines the zero angle. As the light beams are located in small enclosures of their own (visible at the bottom in figure 1(b)), their position cannot be measured directly. However, from the timestamps of both light beams, we can obtain the delay from the reference edge to the first succeeding

control slot edge. This delay is $\left(\Delta\beta - \left\lfloor \Delta\beta\frac{50}{\pi}\right\rfloor\frac{\pi}{50}\right)/\omega$, where ω is the angular frequency of the wheel rotation. An approximate physical measurement was sufficient to determine the integer $\left\lfloor \Delta\beta\frac{50}{\pi}\right\rfloor$ that represents the number of control slots between the two light beams. This resolves the ambiguity and allows determining $\Delta\beta$.

In order to derive β_1 from $\Delta\beta$, two assumptions had to be made: that the light beams' horizontal positions are symmetric with respect to that of the wheel axle; and that their positions in their respective enclosures are the same. Then $2d$ equals the width of one of the enclosures and Δh equals their height difference, both of which are easily measured with a caliper. There remains a one-to-one correspondence between the vertical light beam position h and $\Delta\beta$, which was solved for h with Newton's method. From h, β_1 was computed, which fixes the angle zero relative to the orientation of the mask.

As mentioned in the previous section, the wheel cutouts are not perfectly accurate. With a modified trigger generator circuit, timestamps of all four edges were recorded, and their angles α_1, α_2 and α_3 relative to the reference edge were determined. As before, the reference edge is defined so that $\alpha_2 \geqslant \pi$.

Figure 4(b) shows the piecewise linear function describing the uncovered fraction of the mask opening as a function of the wheel angle, where the angle is zero when the reference edge passes the left light beam. The corner points of the function depend on the determined parameters as specified. The mask cutout angle $\gamma = \frac{5}{12}\pi$.

3. Measurement results

3.1. A cooled snapshot infrared camera

3.1.1. Operation of cooled thermal infrared cameras. A cooled thermal infrared camera works like a video camera in principle. Its detector generates an electrical change proportional to the incident radiation, which is then drained and amplified. It integrates infrared radiation during an integration (exposure) interval and is insensitive outside that interval. The term 'snapshot' refers to the fact that all pixels are exposed at the same time, which is typically the case in cooled infrared cameras.

A pixel value P increases proportionally to the integral of the incident light intensity I over the integration interval:

$$P(t) - P_0 \propto \int_{t+t_\text{delay}}^{t+t_\text{delay}+T} I(s)\,\mathrm{d}s, \qquad (1)$$

where t is the trigger time, t_delay the trigger delay and T the integration time. P_0 is the pixel value in the absence of any incident radiation.

3.1.2. Camera and measurement details. The camera investigated here was an IRcam Equus 327k L MCT PRO containing a Mercury Cadmium Telluride detector with a resolution of 640x512 pixels. The camera outputs 14 bits per pixel.

The integration time was 250 μs. A 50 mm lens with a field of view of 17.5° by 14.0° was used. The distance between camera and chopper wheel was adjusted so that the chopper wheel filled the image and its axle was approximately in the centre.

In the measurement setup, the centre region of the chopper wheel reflects the detector and aperture of the camera, which are cooled down to 60 K. In order to easily distinguish the mask and wheel from the blackbody background, the blackbody was set to a higher than ambient temperature, 30 °C.

The trigger scheme used for the measurements was the one given in section 2.3. The camera frame rate was 30.303 Hz, the chopper wheel rotated with the frequency 3 Hz, and the sampling angle interval was $2\pi/1000$. Each measurement was repeated 20 times, taking 11 minutes.

Infrared imaging detectors require a non-uniformity correction because the thermal characteristics of pixels differ and can change over time. For the IRcam Equus, this has to be done by the user. For that purpose, before or after a timing measurement two recordings of only the blackbody were made, with two temperatures, 15 °C and 30 °C. The camera frames were corrected using these two reference recordings before processing them further.

3.1.3. Processing of image sequences. For each timing measurement, some frames were selected where the mask opening was completely uncovered. A rectangular region of interest (ROI) that contained the opening was selected visually. A histogram of the ROI was generated and a threshold pixel value between the peaks of the foreground and the blackbody background was selected. Then for the whole recorded image sequence, and the number of pixels in the ROI with values above the threshold value was determined.

Since the mask opening extends over 75° and the cutouts of the chopper wheel over 90°, there are two angle intervals each where the opening is completely uncovered or obscured. The location of these intervals can vary depending on a trigger delay. The interval boundaries were determined manually, and corresponding data points averaged to obtain an average minimum and maximum pixel count. The pixel counts between these bounds were then normalised to $[0,1]$, giving the uncovered fraction of the mask opening.

Finally the trigger timestamps were replaced by the corresponding angles determined as described in section 2.4. Opening fractions and angles of all measurement runs were averaged for each nominal wheel angle, and their variation used to obtain an error estimate for both variables.

3.1.4. Relative trigger delays. The simplest demonstration of the measurement method is the determination of differing internal trigger delays of the same camera. As no camera with a variable internal trigger delay was available, this was simulated with the trigger generator. Five timing measurements were made, with trigger delays from zero to 100 ms in steps of 25 ms.

The results are shown in figure 5. The independent variable is the wheel orientation angle at the time of the camera frame triggers, ignoring the trigger delay (which we will determine
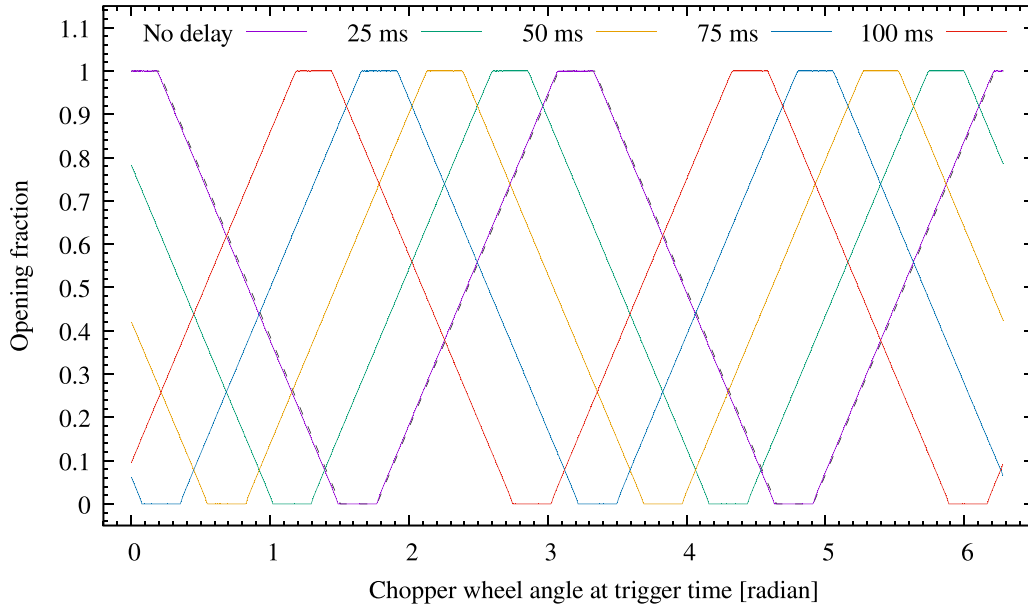
Figure 5. Measurement results for the cooled infrared camera IRcam Equus with different trigger delays. Errors in both variables are smaller than the line thickness. The dashed black line is the model from figure 4(b). Measurements with a larger trigger delay are shifted to the left because the same state of the chopper wheel is seen in frames triggered earlier.

Table 1. Relative trigger delays derived from the data in figure 5 compared to nominal delays set in the trigger generator, error estimates and deviations from nominal values.

Nominal (ms)	Measured (ms)	Uncertainty (μs)	Deviation (μs)
25	24.998	± 1.123	-1.745
50	49.999	± 1.277	-0.652
75	75.003	± 1.083	3.000
100	99.998	± 1.137	-2.021

from the measurements). The plateaus are the intervals during which the mask opening is fully exposed (1) or completely covered (0). The slopes are linear due to the design of the mask cutout and the uniform rotation of the wheel. Successively larger trigger delays shift the plot to the left because earlier triggers correspond to a given wheel orientation.

The relative trigger delays was recovered from the measurements by quantifying the horizontal shift of the different results. First the partial slopes that extend to 2π were wrapped around to negative angles. Then the linear function $1/2 + m\,(x - c)$ was fitted to each slope between the opening fractions 0.05 and 0.95, to exclude the plateaus. By construction c gives the mean horizontal position of the slope regardless of m. The scientific plotting program Gnuplot [24] was used for fitting, which uses the fit method presented in [25].

The relative horizontal positions of the four slopes were averaged to obtain the trigger delay in angular units and, after division by the angular velocity of the wheel, in time units. Table 1 shows the results. The measured trigger delays are quite close to the nominal values, though the errors have been underestimated somewhat.

3.1.5. Absolute trigger delay. The absolute trigger delay of the camera was determined by comparison of the horizontal position of the slopes in the measurement results with the model from section 2.5. All five measurements from the previous section were used, taking the additional nominal trigger delays into account. The results differ between using only falling or only rising slopes:

$$t_{\text{delay, falling}} = (567.74 \pm 2.06)\,\mu\text{s}$$
$$t_{\text{delay, rising}} = (488.91 \pm 2.77)\,\mu\text{s}$$

The cause for this discrepancy is not apparent. It is worth noting that a similar but much smaller effect was found in [12] for a video camera. Though the measurement methods differ, illumination or darkness before triggering is a common factor. Due to the different wavelengths and materials involved in thermal photon detectors and cameras, the imperfection causing the effect may be amplified.

3.2. A microbolometer infrared camera

3.2.1. Operation of microbolometer infrared cameras. Microbolometer infrared cameras have a different operating principle from cooled infrared cameras (see e.g. [26]), which affects their timing. A microbolometer detector consists of pixels suspended above the detector substrate and attached by electrical connections. The pixel value is obtained by measuring the temperature-dependent resistance of the pixel.

The temperature of a detector pixel is influenced by conductive heat exchange with the detector substrate and radiative heat exchange with the part of the scene it sees, its instantaneous field of view. The former process is described by a first-order linear differential equation, Newton's law of cooling.

Due to the limited wavelength interval in which a camera is sensitive and over the temperature interval relevant here, the heat exchange with the scene is very well approximated by another first-order linear differential equation. This will be verified in the following section for the investigated camera.

Then the dependence of the pixel temperature on the scene is described by a first-order linear differential equation that can be written in the form

$$\dot{T}_{\text{pixel}}(t) = \frac{1}{\tau}\left(T_{\text{asymp}}(t) - T_{\text{pixel}}(t)\right), \tag{2}$$

where τ is decay time describing the camera's adaption to a changing scene, one timing parameter we will determine. $T_{\text{asymp}}(t)$ is the temperature the pixel would approach if the scene at time t remained static.

Microbolometer cameras are practically universally rolling-frame cameras, meaning that pixel rows are read out from the detector sequentially. The delay between successive rows is another timing parameter of microbolometer cameras, as is the overall trigger delay. Taking both into account, the pixel value

$$P(t;y) \propto T_{\text{pixel}}\left(t + t_{\text{delay}} + y\,t_{\text{row}}\right), \tag{3}$$

where y is the row coordinate of the pixel, t_{delay} is the trigger delay and t_{row} is the row delay. It is worth noting that due to (2), pixel values are influenced by the scene before the trigger time, in contrast to (1) for cooled cameras.

3.2.2. Camera and measurement details.

The camera investigated was a Jenoptik IR-TCM 640 with a resolution of 640×480 pixels that outputs 16 bits per pixel. A 30 mm lens with a field of view of 30° by 23° was used. The distance between camera and chopper wheel was adjusted so that the chopper wheel filled the image and its axle was approximately in the centre.

The camera detector and lens casing are reflected by the chopper wheel. In contrast to the cooled camera, these are warmer than ambient temperature. So in order to easily distinguish the mask and wheel from the blackbody background, the blackbody was set to a lower than ambient temperature, 15 °C.

To check the validity of (2) in our situation, Planck's law was integrated numerically over the sensitivity range of the camera, from 7.5 to 14 µm. A straight line was fitted to the resulting irradiance $I(T)$ for $T \in [288\,\text{K}, 298\,\text{K}]$. The RMS deviation of the fit was 0.038 W m^{-2}, which is quite small compared to the value range from 48.8 to 57.5 W m^{-2}. So (2) is indeed valid.

The trigger scheme used for the measurements was again the one presented in section 2.3: The camera frame rate was 30.303 Hz, the chopper wheel rotated with the frequency 3 Hz, and the sampling angle interval was $2\pi/1000$. The measurement was repeated 21 times, taking 11.5 mins.

This camera performs its own non-uniformity correction and outputs corrected images. To that end it contains a calibration surface that is moved in front of the detector twice at the start of each recording. The data up to the second such operation were discarded as invalid.

3.2.3. Processing of image sequences.

As for the cooled camera, one main measured quantity is the fraction of the mask cutout not covered by the chopper wheel. In addition, the uncovered fractions of each pixel row of the cutout will be computed in order to determine the row delay.

In contrast to the analysis of the cooled camera measurements, pixel values within the mask opening were added up rather than counting those exceeding a threshold. This was done to catch the intermediate pixel values arising from the decay behaviour.

To that end, some frames were selected where the mask opening was completely uncovered. Using a suitable threshold, a mask image was generated in which only the pixels within the cutout were non-zero.

With this mask image, the sums of pixel values within the mask was computed, both in total and for each pixel row. A linear drift of mean pixel values over the measurement duration was compensated by fitting a straight line and subtracting it.

Pixel sums were normalised using the averages of the extrema of the two upper and lower plateaus, respectively. The normalised results were reversed by $x \mapsto 1 - x$ to account for the cold blackbody background. Figure 6 shows the normalised opening fractions for the whole mask cutout and four selected mask rows. Data points are represented by (very small) error crosses. Uncertainties in both variables were obtained from the variations over the measurement runs. In the camera frame in figure 6(b) the rolling-frame effect causes the vertical chopper wheel edges to bend.

3.2.4. Method of analysis and results.

There are three parameters to be determined: The overall trigger delay, the row delay and the decay time. The experimental data consist of sets of opening fractions by angle, one set for the whole mask cutout and 193 sets for the individual pixel rows within the cutout.

There is no simple way to derive all parameters directly from the data. Therefore a simulation program was written that generates synthetic data from trial parameters, the chopper wheel geometry from section 2.5, the mask image and the wheel centre coordinates. Each sampling interval of $2\pi/1000$ was subdivided by ten simulation steps. The simulated quantities are normalised opening fraction of cutout rows or the whole cutout. As (3), summing pixel values and normalisation are all linear operations, an equation of the form (2) with the same decay time also applies to them. Instead of T_{asymp}, the target of the decay process is the instantaneous opening fraction computed from the current wheel angle and the cutout pixel mask. The differential equation was integrated with the classical Runge–Kutta method.

The row delay was taken into account by advancing the wheel angle appropriately from row to row. This amounts to shifting the time zero for each row and saves having to interpolate between time steps to obtain the results. The opening
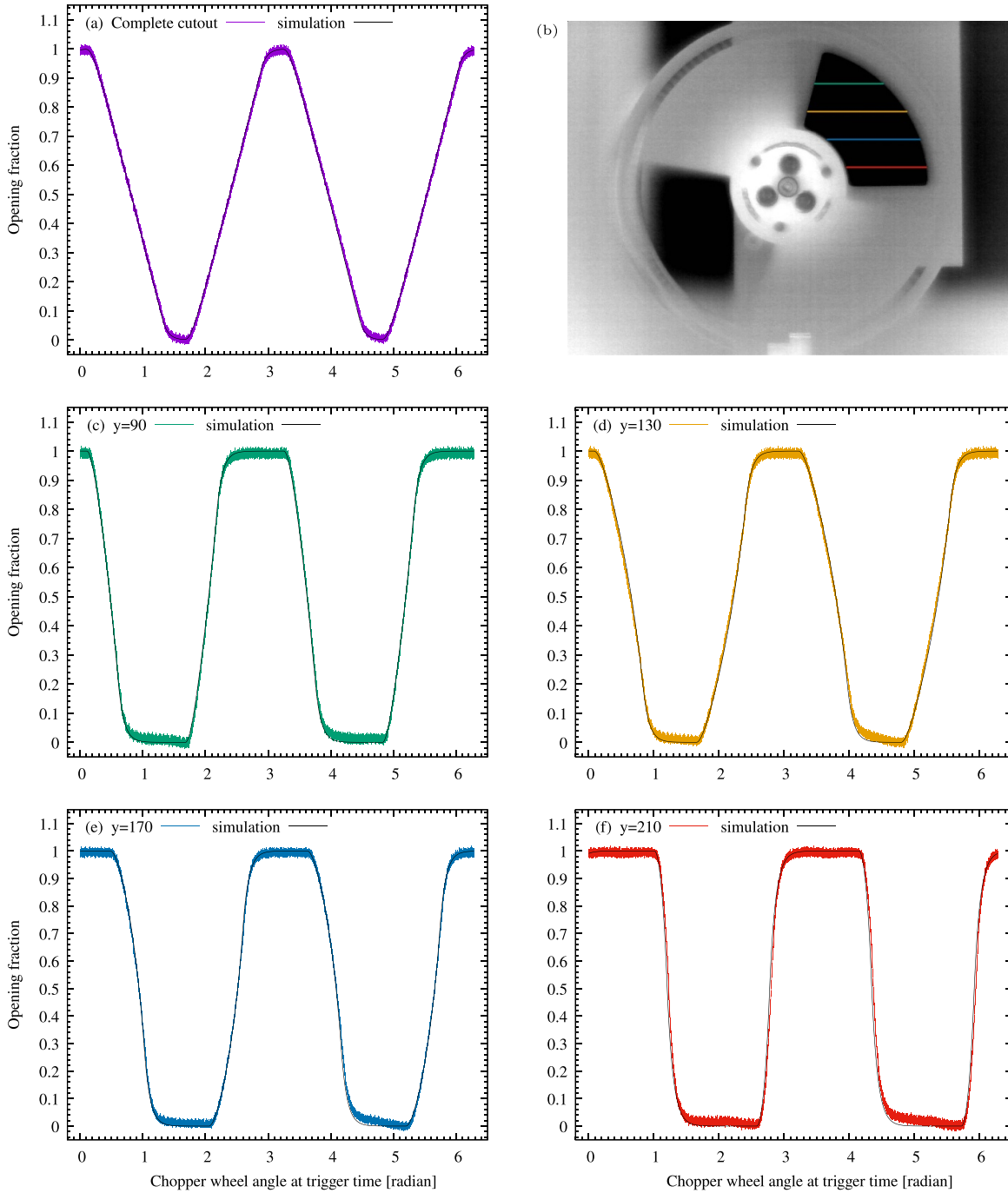
Figure 6. Measurement results for the microbolometer infrared camera Jenoptik IR-TCM 640. (a) Overall opening fractions analogous to the cooled camera results. (c) to (f) Uncovered fractions of selected cutout pixel rows displayed in (b). The black lines are a simulation with the determined timing parameters.

fractions were initialised to 0.5, and two rotations of the wheel were simulated as run-in before a third rotation was simulated and output.

Given a simulation result and the experimental data, corrections for the delay of each pixel row were determined by averaging the horizontal distance of slopes between opening fractions of 0.2 and 0.8. Fitting a straight line to the delays of the row data depending on the y coordinate yields corrections to the overall trigger delay (the intercept) and the row delay (the slope). The simulation and delay determination was

repeated three times to obtain an accurate consistent parameter set.

This was done for a range of equidistant decay times. A plausible value range was determined by fitting a decaying exponential to the start of a slope in the measured data. The initial trigger delay was set to zero, and the initial row delay, $1/f_{max}/480$ was chosen, where f_{max} is the maximum frame rate of the camera and 480 is the vertical image resolution. The RMS deviation from the measurement results was determined over all data sets for the selected decay times. A parabola

was fitted to the deviations as a function of the decay time to determine the optimum. The other two timing parameters were then determined as above. The optimal parameter set is:

$$\tau = 4.819 \text{ ms}$$
$$t_{\text{delay}} = 3.872 \text{ ms}$$
$$t_{\text{row}} = 38.76 \text{ µs}$$

The uncertainty obtained for the decay time from the parabola fit was of the order of nanoseconds and is almost certainly an underestimation. A simulation with this parameter set is displayed in black in figure 6, which fits the measurement quite well. The major uncertainties of the measurement method are likely to result from imperfections of the setup rather than inaccuracies of the analysis and will be discussed in the following section.

4. Discussion

The previous sections have presented example results of measured timing parameters of thermal infrared cameras. This section will take a look at sources of errors and possible variants and improvements.

The method relies on the chopper wheel as a mechanical reference, which comes with greater inaccuracies than one using only electronics such as [12] for video cameras. As described in section 2.4, the timestamps of the control slot edges are used to compensate some variations in rotation speed. But the control slots are also not perfectly regular. Viewing the signals from both edge detectors with an oscilloscope shows that the time interval from the last control slot before the cutout edge is not the same in both halves of the wheel but differs by 26 µs. Also, the deviations of the control slot timestamps from regularity are not random, but show a repeating pattern. Irregularities in the angles of the control slot edges could be the cause.

That the angles of the cutout edges are not perfectly accurate has been measured and corrected according to section 2.5. But the assumption that the edges of the outer ring edges (visible in figure 1(b)) match the edges of the cutout has not been verified. The differences between the two lower plateaus in figures 6(d)–(f) indicates that the two leading edges differ and may not be perfectly straight or radial.

The only way to ameliorate these effects would be to manufacture a chopper wheel to more accurate specifications than commercially available. Using a physical process such as a pendulum as a mechanical reference could also be considered if it was suitably timed with light beams.

The effect of a potential lens distortion has been minimised with limited effort by approximately aligning the optical axis with the wheel centre, see section 2.1. If the lens distortion were determined in a geometrical calibration, the effects of lens distortion could be compensated. The cutout could then also be recorded full-frame, obtaining more data and statistical significance.

To obtain the microbolometer camera results, we have used the linear dependence of the irradiance over the wavelength

sensitivity range on the temperature. This is no longer true over a larger temperature range. The slope of the dependency rises by a factor 1.6 from 273 K to 323 K. A second measurement at a different 10 K interval together with the integral of the Planck law would allow to determine separate time constants for the heat exchange of pixels with the detector substrate, and with the scene. However, a simulation over a larger temperature range would require integrating a non-linear differential equation instead of (2).

5. Summary and outlook

This work has presented a measurement method characterising the timing behaviour of thermal infrared cameras by determining a number of parameters. It is equally suitable for both cooled and microbolometer cameras, and for both snapshot and rolling-frame cameras.

The accuracy of the measured trigger delays has been demonstrated with a snapshot cooled camera operated with different trigger delays. The suitability for microbolometer cameras has been shown in an investigation of such a camera. The accuracy of those results has been demonstrated with a simulation based on the determined parameter set.

The measurement setup consists primarily of commercially available components. Exceptions are the machined mask plate and the 3D-printed bases for orienting the cameras and the chopper head. As presented in the discussion, improvements in accuracy could be achieved by manufacturing components specifically for this method, notably the chopper wheel. Geometrically calibrating the camera lens with a suitable model and extending the microbolometer camera simulation to a larger temperature range has also been left to future work.

Data availability statement

The data that support the findings of this study are available upon reasonable request from the authors.

ORCID iD

Volker Schatz ● https://orcid.org/0000-0002-7326-7035

References

[1] Svanström F, Englund C and Alonso-Fernandez F 2021 Real-time drone detection and tracking with visible, thermal and acoustic sensors *25th Int. Conf. on Pattern Recognition (ICPR)*

[2] Zhu J, Yusheng X, Zhen Y, Hoegner L and Stilla U 2021 Fusion of urban 3D point clouds with thermal attributes using MLS data and TIR image sequences *Infrared Phys. Technol.* **113** 103622

[3] Borgmann B, Schatz V, Hammer M, Hebel M, Arens M and Stilla U 2021 The MODISSA testbed: a multi-purpose platform for the prototypical realization of vehicle-related applications using optical sensors *Appl. Opt.* **60** F50–F65

[4] Milella A, Reina G and Nielsen M 2021 A multi-sensor robotic platform for ground mapping and estimation beyond the visible spectrum *Precis. Agric.* **20** 423–44

[5] Shimoda M, Sada Y, Kuramochi R and Nakahara H 2019 An FPGA implementation of real-time object detection with a thermal camera *29th Int. Conf. Field Programmable Logic and Applications (FPL)* pp 413–4

[6] Leira F S, Helgesen Håkon H, Johansen T A and Fossen T I 2021 Object detection, recognition and tracking from UAVs using a thermal camera *J. Field Robot.* **38** 242–67

[7] Khattak S, Papachristos C and Alexis K 2019 Visual-thermal landmarks and inertial fusion for navigation in degraded visual environments *2019 IEEE Aerospace Conf.* (IEEE) pp 1–9

[8] Rosser K 2021 Tran Xuan Bach Nguyen, Philip Moss and Javaan Chahl. Low complexity visual UAV track navigation using long-wavelength infrared *J. Field Robot.* **38** 882–97

[9] Farooq M A, Shariff W and Corcoran P 2022 Evaluation of thermal imaging on embedded GPU platforms for application in vehicular assistance systems (arXiv: 2201.01661)

[10] Ding M, Zhang X, Chen W-H, Wei Li and Cao Y-F 2019 Thermal infrared pedestrian tracking via fusion of features in driving assistance system of intelligent vehicles *Proc. Inst. Mech. Eng.* G **233** 6089–103

[11] Masson L, Cao Féric, Viard C and Guichard Féric 2014 Device and algorithms for camera timing evaluation *Proc. SPIE* **9016** 90160G

[12] Schatz V 2017 Measurement of the timing behaviour of off-the-shelf cameras *Meas. Sci. Technol.* **28** 045905

[13] Lai H W and Tsui C M 2021 Calibration of timing parameters of still image cameras and video cameras by a two dimensional LED array *NCSL Int. Measure* **13** 23–35

[14] Hopkinson G, Rojas L G, Skipper M and Meynart R 2008 Testing of InGaAs, microbolometer and pyroelectric detectors in support of the EarthCARE mission *Proc. SPIE* **7106** 71061O–8

[15] Danial A N 2013 Using high speed shutter to reduce motion blur in a microbolometer *Bachelor Thesis* (available at: www.diva-portal.org/smash/get/diva2:1021488/FULLTEXT02)

[16] Peeters J, Louarroudi E, De Greef D, Vanlanduit S, Dirckx J J J and Steenackers G 2017 Time calibration of thermal rolling shutter infrared cameras *Infrared Phys. Technol.* **80** 145–52

[17] Waldron D L and Lohrmann D J 2020 Per-pixel time constant measurement of bolometer cameras *IEEE Trans. Instrum. Meas.* **69** 7725–39

[18] Lambkin P, Folan N and Lane B 1999 Simple technique for the measurement of thermal time constants of microbolometer structures *Proc. 1999 Int. Conf. Microelectronic Test Structures* pp 179–83

[19] Tu X, Xu L, Mao Q, Wan C, Kang L, Jin B, Chen J and Peiheng W 2014 Quasioptical terahertz detector based on the series connection of Nb5N6 microbolometers *J. Appl. Remote Sens.* **8** 084992

[20] Svatos V, Gablech I, Pekárek J, Klempa J and Neuzil P 2018 Precise determination of thermal parameters of a microbolometer *Infrared Phys. Technol.* **93** 286–90

[21] Tsai R Y 1987 A versatile camera calibration technique for high-accuracy 3D machine vision metrology using off-the-shelf TV cameras and lenses *IEEE J. Robot. Autom.* **RA-3** 323–44

[22] Hartley R and Zisserman A 2003 *Multiple View Geometry in Computer Vision* 2nd edn (Cambridge: Cambridge University Press)

[23] The PARI Group, Univ. Bordeaux 2019 PARI/GP version 2.13.3 (available at: http://pari.math.u-bordeaux.fr/)

[24] Gnuplot (available at: www.gnuplot.info/)

[25] Orear J 1982 Least squares when both variables have uncertainties *Am. J. Phys.* **50** 912

[26] Vollmer M and Klaus-Peter M 2010 *Infrared Thermal Imaging: Fundamentals, Research and Applications* (New York: Wiley)